

Dark matter constraint with γ -ray galaxies cross correlation scales with N

Daiki Hashimoto*

*Division of particle and astrophysical sciences, Graduate School of Science,
Nagoya University, Furocho Chikusa, Nagoya, 464-8602, Aichi, Japan*

Atsushi J. Nishizawa

*Division of particle and astrophysical sciences, Graduate School of Science,
Nagoya University, Furocho Chikusa, Nagoya, 464-8602, Aichi, Japan
Institute for Advanced Research, Nagoya University,
Furocho Chikusa, Nagoya, 464-8602, Aichi, Japan*

Masahiro Takada

*Kavli Institute for the Physics and Mathematics of the Universe (WPI),
The University of Tokyo Institutes for Advanced Study (UTIAS),
The University of Tokyo, 5-1-5 Kashiwanoha, Kashiwa-shi, Chiba, 277-8583, Japan*

Oscar Macias

*Kavli Institute for the Physics and Mathematics of the Universe (WPI),
University of Tokyo, Kashiwanoha, Chiba, 277-8583, Japan
GRAPPA Institute, Institute of Physics, University of Amsterdam, 1098 XH Amsterdam, The Netherlands
(Dated: September 21, 2021)*

A new method to constrain the dark matter annihilation cross section by taking the cross correlation of γ -ray diffuse maps and galaxies is proposed. As a result, the statistical power of constraining the annihilation cross section is proportional to the galaxy mass and the inverse square of the distance to the galaxy. Therefore, for analyses using dwarf galaxies, the measurement of the distance to the dwarf galaxies is crucial for stringent constraints. However, measuring the distance to galaxies is, in general observationally expensive, particularly for faint or diffuse galaxies. Under the situation of stacking N galaxies, we show that the distance to the individual galaxy measurement is not required, but the overall distance distribution is sufficient for the cross section constraints. Further, based on real Large Area Telescope (LAT) data, we show that the effect of covariance between two galaxies located closely, typically comparable with the point spread function size of the *Fermi*-LAT, is negligibly small. We can independently stack the likelihood for the N galaxies, which dramatically reduces the computation costs. By using actual datasets of the LAT γ -ray sky and ~ 800 faint objects discovered by Hyper Suprime-Cam, we find that the upper limit on the annihilation cross-section scales with $1/N$. Therefore, it can be one of the most powerful and robust probe of the annihilation signal to stack more than 10^5 galaxies readily available with the Legacy Survey of Space and Time.

I. INTRODUCTION

In the last several decades, revealing the nature of dark matter (DM) has been a major challenge in modern cosmology and particle physics. As one of the most theoretical-motivated candidates for the DM of dominant fraction, weakly interacting massive particles (WIMPs) have been considered [1] and probed via different approaches by colliders, underground experiments and astronomical observations [e.g. 2, 3]. In the context of astrophysics, researchers often focus on probing signals from the self-annihilation or decay of WIMPs. In the early universe, WIMPs are considered to be produced in thermal equilibrium with standard model (SM) particles. As these interact with each other, WIMPs can annihilate into SM particles, particularly heavy SM particles, such as $b\bar{b}$ and W^+W^- [4, 5]. As assumed that WIMPs are

of DM abundance in the Universe, WIMP were reported to have an annihilation cross-section of $\sim 2 \times 10^{-26} \text{cm}^3/\text{s}$ in the DM mass range while trying to elucidate the DM abundance, which is known as the thermal relic cross-section [6]. As a result of the annihilation process, γ rays can be produced directly or in secondary cascades that more massive states decay into more stable ones, particularly photons, electrons, positrons and neutrinos. Therefore probing these particles induced by DM annihilation gives clues to specify DM properties.

The Fermi Large Area Telescope (LAT) has revealed the γ -ray sky over more than a recent decade in the energy range from 20 MeV to 1 TeV. In the fourth γ -ray source catalog by the *Fermi* collaboration [7], the most detailed galactic diffuse emission was reported and point-source catalog containing about 5,000 objects with above 4σ detection level have been resolved. In addition, more than 3,700 sources have been found to have identified or associated counterparts of pulsars, supernova remnants and blazars. These results allow us to probe the DM annihilation signal from the galactic centre and halo [8–

* hashimoto.daiki@f.mbox.nagoya-u.ac.jp

13]. As another interesting component of the observed emission, there is residual emission obtained by subtracting the resolved point-source and galactic diffuse emission from observational data. It is interpreted as γ rays from unresolved extragalactic sources and is accordingly named as unresolved γ -ray background (UGRB), which has been studied to probe the annihilation signal by combining several low-redshift object catalogs for galaxies, galaxy groups and galaxy clusters [14–20]. The galactic and extragalactic targets have numerous γ -ray sources of astronomical origins. For robustness of the search for very faint signals, it is imperative to avoid contamination of γ -ray photons from astronomical sources in target objects. The search for γ -ray emission from Milky Way dwarf spheroidals (dSphs) is a robust DM probe [21–26] because Milky Way dSphs are expected to have quiescent star-formation activities; thus, they have less γ -ray emission from a star-formation region, pulsar and supernova remnant. Using 27 dSphs in our galaxy, [26] have an upper limit of the DM annihilation cross-section as $\sim 3 \times 10^{-27} \text{cm}^3/\text{s}$ at a 10 GeV DM mass with 95% C.L., which was much smaller than the thermal relic cross-section.

In our previous work [27], a low-surface-brightness galaxy (LSBG), which has less than $\sim 23 \text{ mag/arcmin}^2$ mean surface brightness, has been proposed as a new target to probe the DM annihilation signal in UGRB. LSBGs are known to be highly dominated by DM [28, 29] and have more massive halos than Milky Way dSphs, $\sim 10^9 M_\odot$. Further, they have less star-formation activities and γ -ray emission from pulsars and supernova remnants than ordinary galaxies or galaxy clusters [30]. However, owing to their faint fluxes, it is more difficult to measure their redshifts than ordinary galaxies. Therefore, in our previous work, we used an LSBG catalog constructed by [31] using the Hyper Suprime-Cam (HSC) data. Although this catalog contained ~ 800 objects, we could only use eight LSBGs with precisely measured redshift because of the unknown redshifts of other objects.

In this study, we propose a method to access a large number of objects without knowing their redshifts for probing the DM annihilation signal. We focus on the redshift distribution of an entire catalog instead of the redshifts of individual objects. For measuring the redshift distribution, we apply the redshift clustering method [32–34]. To validate the proposed method, we demonstrate the redshift clustering method and a composite likelihood analysis for probing the DM annihilation signal using full samples of the HSC-LSBG catalog and the UGRB emission constructed from γ -ray observation data by the *Fermi*-LAT. To reduce the computational cost, in the likelihood analysis we assume that all γ -ray components for the LSBGs are independent; however, in fact neighboring objects correlate because their mean angular separation is smaller than the point spread function (PSF) of the *Fermi*-LAT in an energy level lower than a few GeV. Therefore, we verify our assumption by estimating covariance on the model parameters of neighboring

objects. We also discuss the power of stacking numerous objects in the likelihood analysis. Because LSBGs are potentially abundant in the local universe, some extremely deep galaxy surveys by next-generation telescopes such as the Legacy Survey of Space and Time (LSST), are planned in the future; a significant number of LSBGs will be discovered. Then LSBGs can be the most desirable target for the indirect search of the DM annihilation signal.

This paper is organized as follows. In Section II, we visit the method of γ -ray emission modeling for target objects and the redshift clustering method. In Section III, we demonstrate the proposed approach using HSC-LSBGs and *Fermi*-LAT data. We present a scaling relation of constraint on the DM annihilation with N_{st} objects in Section IV. Finally, we conclude this study in Section V.

II. THEORETICAL FRAMEWORK

In this section, we present our approach to constrain the DM annihilation cross-section using cross-correlation between diffuse γ -ray background and the massive nearby objects expected to be highly DM dense regions, such as dSphs, faint galaxies and normal galaxies, without no individual distance measurement. For the analysis feasibility, we require an overall probabilistic distribution of the objects along the line of sight.

Here, we assume that all objects are statistically independent, which dramatically simplifies the stacking likelihood analysis. In Subsection IV A, we evaluate the validity of this assumption.

A. γ -ray flux modeling for DM annihilation

Through the DM annihilation process, γ -ray photons are generated directly or in the cascade process in which various final states (e.g. $b\bar{b}$, W^+W^- and $\mu^+\mu^-$) decay into more stable particles. The γ -ray flux $d\Phi_{\text{ann}}/dE$ produced by DM annihilation can be modeled as follows,

$$\frac{d\Phi_{\text{ann}}}{dE} = J \times \frac{\langle \sigma v \rangle}{8\pi m_\chi^2} \sum_i \text{Br}_i \frac{dN_i}{dE}, \quad (1)$$

where m_χ is the DM mass and $\langle \sigma v \rangle$ is the average DM annihilation probability. Br_i and $\frac{dN_i}{dE}$ are the branching ratio and γ -ray energy spectrum of γ -ray photon in the i -th annihilation channel, respectively. In the analysis, we consider $b\bar{b}$ as a representative annihilation channel and obtain $dN_{b\bar{b}}/dE$ by DMFIT¹ [35] included in the LAT

¹ https://fermi.gsfc.nasa.gov/ssc/data/analysis/scitools/gammamc_dif.dat

science tool, **fermipy**. J is the so-called J-factor, which is characterized by DM halo properties as follows,

$$J = [1 + b_{\text{sh}}(M_{\text{halo}})] \int_s ds' \int_{\Omega} d\Omega' \rho_{\text{DM}}^2(s', \Omega'), \quad (2)$$

where s' , Ω' and M_{halo} are the line-of-sight vector, solid angle and halo mass of target objects, respectively. The annihilation signal may increase if we have clumpy substructures within a halo instead of the smooth halo. This can be effectively modeled as a boost factor, b_{sh} [36]. For clarity, we set $b_{\text{sh}} = 1$ for all mass-scale halos throughout this paper. The DM density profile is assumed to follow the Navarro-Frenk-White (NFW) profile [37],

$$\rho_{\text{DM}}(r) \propto \frac{1}{cr/r_{\text{vir}} [(cr/r_{\text{vir}}) + 1]^2}, \quad (3)$$

where $c(M_{\text{halo}})$ is the concentration parameter. The concentration parameter primarily depends on the halo mass and we compute it using the fitting formula to model the scaling relation of $c(M)$ with halo mass, calibrated using the high-resolution N-body simulations [38]. We convert the halo mass to the concentration by using **COLOSSUS** [39].

The full description of J-factor estimation can be found in [27]. A brief summary is as follows. We first convert the observed magnitude into the absolute magnitude. The V-band apparent magnitude can be converted from the gri system as $V = g - 0.59(g - r) - 0.01$ [40]. Now, the situation is that we do not have the distance to individual galaxies but an overall distribution. However, we can formally write the distance of each galaxy as a random draw from the distribution: $d \in dN/dz(z)$. For the particular realization of the random draw of the distance with the binding condition of $\langle d \rangle = dN/dz$, the absolute magnitude can be computed; thus, the halo mass can be derived by assuming the relations of mass-to-light ratio [41] and stellar to halo mass ratio [42].

Given that we have the overall dN/dz distribution, with measurement errors, we can simulate the effect of neglecting distance to individual galaxies. Figure 2 shows the distribution of the total J-factor after stacking N_{st} galaxies. For this plot, we use the HSC-Y1 LSBG sample, where no distance is available. The N_{st} LSBGs are randomly selected from the parent sample 500 times. The scatter in the figure correspond to the 95% ranges due to the sample variance.

B. Measurement of the redshift distribution of photometric samples

In this subsection, we describe a method to estimate the dN/dz distribution from spatial clustering, so called the clustering redshift method. The application of the method to the data is shown in Subsection III C.

Given two galaxy samples in an overlapped region. Even if the galaxies in the two galaxy samples are statistically different, they both correlate with the underlying

DM distribution. In the case where one galaxy sample has known redshifts and the other has unknown redshifts, taking the cross-correlation between the two galaxy samples gives a statistical estimate of the redshift distribution of the galaxies with unknown redshifts. We denote the galaxy samples with known and unknown redshifts as ‘*spectroscopic sample*’ and ‘*photometric sample*’, respectively. The angular cross-correlation function can be factorized as follows [32],

$$w(\theta) = \int_0^\infty dz \frac{dN_p}{dz} \frac{dN_s}{dz} b_p(z) b_s(z) w_{\text{DM}}(z, \theta), \quad (4)$$

where subscripts ‘ s' ’ and ‘ p' ’ represent spectroscopic and photometric samples, respectively. $\frac{dN}{dz}$ represents the redshift distribution normalized to unity, $b(z)$ is a linear bias, and $w_{\text{DM}}(z, \theta)$ is the angular DM correlation function. Notably, the mass of the employed DM model is high enough not to affect the DM clustering pattern itself. We define an integrated cross-correlation \bar{w} with a weighting function $W(\theta)$ as follows

$$\bar{w} = \int_{\theta_{\text{min}}}^{\theta_{\text{max}}} d\theta W(\theta) w(\theta), \quad (5)$$

where the weight W is introduced so that the signal to noise ratio of \bar{w} can be optimised. Following [33], we empirically adopt $W = \theta^{-1}$. In practical measurement, we divide the spectroscopic sample into narrow redshift bins so that dN_s/dz can be approximated by the narrow top-hat function; $dN_s^i/dz \simeq 1/\Delta z$ if $z_i < z < z_{i+1}$. Now we rewrite Equation 5 at $z = z_i$ as follows

$$\bar{w}(z_i) \approx \frac{dN_p}{dz}(z_i) b_p(z_i) b_s(z_i) \bar{w}_{\text{DM}}(z_i), \quad (6)$$

where $\bar{w}_{\text{DM}}(z)$ can be defined similarly as Equation 5 by replacing $w(\theta)$ with $w_{\text{DM}}(z, \theta)$. This is fully predictable from the standard cold DM theory including the non-linear matter clustering evolution. Otherwise, $w(\theta)$ can be treated as a *constant* if the range of the redshift over which we are going to estimate is small enough. A better estimation might be to replace $w(\theta)$ with the square of the linear growth factor, $D^2(z)$. Before concluding to directly connect measurement to the dN_p/dz , we need to address the bias functions. The bias of the spectroscopic sample b_s can be measured using the sample auto-correlation. The redshift evolution of the photometric sample b_p is fully degenerated with the dN_p/dz and cannot be further decomposed. In this study, we assume the redshift evolution of the bias can be negligible as the redshift range is small $0 < z < 0.15$.

III. RESULT

To validate the proposed method, we applied it to the LSBG samples [31] observed with the HSC survey. The 781 LSBG samples in $\sim 200 \text{ deg}^2$ of the HSC region do

not have individual distance measure, but we have the spec- z samples from NASA Sloan Atlas (NSA) [43] on an almost fully overlapped sky area. Using γ -ray background sky constructed from the *Fermi*-LAT data, we demonstrated the composite likelihood analysis for probing the DM annihilation signal with all HSC-LSBGs using given individual redshift by random draw from measured dN/dz .

A. Data

1. HSC-LSBG catalog

HSC is a wide-field camera, attached to the prime focus of the Subaru telescope, covering $\sim 1.5^\circ$ diameter field of view with 0.17 arcsec pixel scale [44, 45]. The HSC Subaru Strategic Program survey consists of three layers, wide, deep and ultra-deep layers; the wide layer has five broad photometric bands g, r, i, z and y . As described in a report of the second data release of the survey by [46], the wide layer has a depth of 24.5–26.6 in the 5 filters for 5σ point-source detection. In the final data release, the survey will cover 1400 deg² sky in a depth of $i \sim 26$ mag.

Since the HSC pipeline, **hscpipe**, is not optimized for detecting and measuring diffuse objects, HSC images are reduced first by the **hscpipe** and then **SExtractor** is used for detection and measurements. [31] processed an HSC dataset with three broad bands (g, r and i) on a patch-by-patch basis over ~ 200 deg² and produced a catalog comprising 781 LSB objects, which have a mean surface brightness in g -band > 24.3 mag/arcsec². Briefly, the following processes have been executed: (i) bright sources and associated diffuse lights are subtracted from images to avoid contamination to LSB objects detection; (ii) after the Gaussian smoothing with full depth at half maximum of $1''$, sources with the half-light radius $r_{1/2}$ satisfying $2.5'' < r_{1/2} < 20''$ are extracted; (iii) the sources are selected by applying reasonable color cuts to remove optical artifacts and distant galaxies; (iv) by modeling the surface brightness profiles of LSBG candidates, astronomical false positive are removed; (v) by visual inspection, false candidates such as point-sources with diffuse background lights are removed and then 781 LSBGs are finally left.

To minimize a possible contamination of astrophysical γ -ray photons, it might be useful to restrict our analysis to quiescent galaxies, because such galaxies do not have ongoing star-formation activities and therefore unlikely contain high-energy astrophysical sources such as supernova remnants and AGNs, at least compared to star-forming blue galaxies. We divide the sample into red and blue LSBGs, where red is defined by $g - i \geq 0.64$ and blue $g - i < 0.64$, which include 450 and 331 objects, respectively. This color selection roughly corresponds to the galaxy age of 1 Gyr for a $0.4 \times$ solar metallicity galaxy [31]. For a random catalog corresponding to the LSBG catalog, we employ the random catalog of the

HSC photometric data, and randomly resample it such that the number density is roughly 10 times larger than the LSBG density. We also apply the bright star mask to the random catalog.

2. NSA sample

For measuring the dN/dz distribution, we need reference spec- z samples in the overlapped region in both sky-coverage and redshift range. Since the LSBGs are likely detected in the nearby universe, we need a low-redshift spec- z sample. The NSA sample² is a spec- z sample obtained from the spec- z campaign of the Sloan Digital Sky Survey with the Galaxy Evolution Explorer data for the energy spectrum of the ultraviolet wavelength and includes objects up to $z = 0.15$. Since the uniformity of the NSA sample is not guaranteed, we attempt to mitigate the non-uniformity as follows. First, we remove the sample from both HSC and NSA in the bright star masked regions. We checked that, after removing the masked regions, the local number density of NSA galaxies smoothed with each HSC patch has a uniform distribution in most areas of the HSC regions we are working on, except for the low-density region in the VIMOS-VLT Deep Survey (Dec. >1). We generate random catalog including about 10 times more objects than that of the NSA galaxies. In addition, we removed the edge regions in the HSC survey footprint for safety, because the exact survey window near the boundaries is difficult to define.

3. Fermi-LAT data

For γ -ray data to probe the DM annihilation signal, we analyze *Fermi*-LAT Pass 8 data obtained from 2008-08-04 to 2016-08-02, which is the latest version of the entire mission dataset based on the updated reconstruction algorithms [47]. In this subsection, we describe how we reduce the raw γ -ray photon count to the scientifically usable maps where the contributions from point sources and galactic foreground emissions are removed. As recommended by the Fermi collaboration,³ we select the photon event class **P8R3_SOURCE** [48], as the photon count data, which is the most suitable class for the point-source analysis. In addition, we apply the following selections, **DATA_QUAL** >0 , **LAT_CONFIG** $==1$ and **P8R3_SOURCE_V2**, as the corresponding filter expression and the instrument response function for the event class, respectively. We use the photon count in the energy range from 500 MeV

² https://data.sdss.org/sas/dr13/sdss/atlas/v1/nsa_v1_0_1.fits

³ https://fermi.gsfc.nasa.gov/ssc/data/analysis/documentation/Cicerone/Cicerone_Data_Exploration/Data_preparation.html

to 500 GeV with 24 logarithmically spaced energy bins and 0.1° spatial grid size. In all energy bins, the width of each bin is considered to be larger than the energy dispersion, and we require intervals of each spatial bin to be smaller than the LAT PSF at all considered energy ranges. The lower energy scale is determined to balance two opposing effects. If we lower the energy scale, photons around bright sources likely leak due to the broadening of PSF, but if we increase the scale, the number of photons available decreases. For the upper limit, we consider that the LAT performance decreases in an energy regime higher than 500 GeV.

For the composite analysis described in Subsection III B, we select 29 patches whose centers are located in the HSC regions with the separation of at least 3° from each other and individual patches having $10^\circ \times 10^\circ$ sky coverage. Moreover, to avoid contaminating the γ -ray photons produced by the Earth's atmosphere interaction with high energy cosmic rays, we exclude the photon data with zenith angles greater than 100° . In the LAT data analysis, we use `fermipy` (v1.0.1)⁴ [49], which is an open-source software package based on the `Fermi Science Tools` (v2.0.8)⁵

4. UGRB construction and putative flux

To obtain the likelihood profile for the UGRB flux at the position of each LSBG for the composite likelihood analysis, following [21], we revisit the procedure to construct the background and estimate the profile at the LSBG position.

First, for constructing a UGRB, we perform maximum likelihood analysis in each patch to optimize the normalization and spectral parameters of flux models for all sources without our LSBGs in the patch, including the galactic diffuse emission, isotropic emission and detected sources by *Fermi*-LAT. To derive the flux models of all sources above, for the galactic and isotropic emission models, we adopt the standard (`gll_iem_v07.fits`) and the isotropic emission template (`iso_P8R3_SOURCE_V2_v01.txt`)⁶, respectively. The isotropic template represents isotropic contributions from undetected extragalactic sources and residual cosmic ray emission. We also derive resolved point-source models from the 4FGL catalog [7]. Notably, we confirm the nonexistence of any additional point source of test statistics (TS) larger than 25 in our patches.

After the UGRB construction by subtracting the model emissions from the observed flux, we estimate the background flux in each energy bin at the LSBG position to assess a putative flux of our LSBG. According to the

prescription described in the 2FGL catalog, the Bayesian method [50] should be applied for the likelihood analysis of very faint sources [51]. To measure the UGRB flux at the position of each object energy bin-by-bin, we assume a power-law model with normalisation parameter $\alpha_{i,j}$, $d\Phi/dE = \alpha_{i,j}(E/1\text{GeV})^{-2}$, as the i -th LSBG flux model in the j -th energy bin. Here we define TS as $TS = -2\Delta \log \mathcal{L}$ and $\Delta \log \mathcal{L}$ is given as follows;

$$\Delta \log \mathcal{L} = \log \mathcal{L}(\mathcal{D}, \Theta | \alpha_{i,j} = 0) - \log \mathcal{L}(\mathcal{D}, \Theta | \alpha_{i,j}^{\max}), \quad (7)$$

where \mathcal{D} and Θ are the LAT data and the nuisance parameters of flux models for all γ -ray sources except for our LSBGs, which is fixed by the maximum likelihood runs when constructing the UGRB field; $\alpha_{i,j}^{\max}$ is a value when $\log \mathcal{L}(\mathcal{D}, \Theta | \alpha_{i,j})$ is the maximum value and $\alpha_{i,j} = 0$ means no target source. We confirm that TS values at all LSBG locations in the UGRB are less than 1 in most energy bins, which shows validity of adopting the Bayesian method following the way in [7]. In Subsection III B, we perform a composite likelihood analysis with all HSC-LSBGs based on the Bayesian method using the flux likelihood of each LSBG in Equation 7 as priors.

B. Composite analysis

As described in Subsection III A 4, because of the very low γ -ray emission signal for our LSBGs, we apply the Bayesian method for the likelihood analysis, which is performed following the same approach of our previous work [27]. In the computation of the 95% C.L. the upper limits of the DM annihilation cross-section, we employ the Bayesian method for the analysis of faint objects. Since all likelihood values obtained at each object are assumed to be independent of each other, the composite likelihood \mathcal{L}_{st} for the full sample of targets can be expressed as follows;

$$\log \mathcal{L}_{\text{st}}(\alpha | \langle \sigma v \rangle, J) = \sum_{i,j} \log \mathcal{L}_{i,j}^{\text{ann}}(\alpha_{i,j} | \{ \langle \sigma v \rangle, J_i \}), \quad (8)$$

where J_i is the J -factor of the i -th target and the index j runs over all energy bins. $\mathcal{L}_{i,j}^{\text{ann}}$ is the log-likelihood value for the i -th LSBG, which is obtained from the delta-likelihood in Equation 7 by substituting an normalization parameter which corresponds to the flux amplitude of $d\Phi_{\text{ann}}/dE(\langle \sigma v \rangle, J_i)|_{E=E_j}$ to $\alpha_{i,j}^{\max}$.

Now we calculate the J -factor for each object to evaluate the model flux described in Subsection II A. For the simplicity of Equation 2, we need to consider the relationship between the PSF of the LAT instrument and the angular size of objects. The PSF (68% containment angles) decreases from $\sim 1.5^\circ$ to $\sim 0.1^\circ$ as γ -ray energy increases from 500 MeV to 500 GeV. The angular size of LSBG is smaller than a few 10 arcsecs, hence smaller than the PSF in all energy bands. Therefore, we can consider them as point-like sources in the likelihood procedures. Then, the integration of ρ_{DM}^2 over the target

⁴ <https://fermipy.readthedocs.io/en/latest/>

⁵ <https://fermi.gsfc.nasa.gov/ssc/data/analysis/software/>

⁶ <https://fermi.gsfc.nasa.gov/ssc/data/access/lat/BackgroundModels.html>

volume in Equation 2 is reduced to;

$$\int ds \int d\Omega \rho_{\text{DM}}^2(s, \Omega) \rightarrow \int dV \rho_{\text{DM}}^2(r)/d_A^2, \quad (9)$$

where d_A is the angular diameter distance to the object, which is given by assignment of distance randomly drawn followed the measured dN/dz distribution. Then, Equation 9 is straightforwardly calculated; finally, we can write Equation 2,

$$J = (1 + b_{\text{sh}}) \frac{M_{\text{halo}}}{d_A^2} \frac{\Delta \rho_{c,z} c^3}{9} \times \left[1 - \frac{1}{(1+c)^3} \right] \left[\log(1+c) - \frac{c}{1+c} \right]^{-2}. \quad (10)$$

Since our targets are regarded as point sources, our assumption is correct if the angular separations between objects are larger than the LAT PSF over all considered energy ranges; otherwise, it is incorrect because their mean surface number density is about 4 per deg^2 . We will further discuss the parameter correlation between neighboring objects in Subsection IV A. In our procedure, we assume that the LSBG flux is positive definite, which implies that the data are well-described by a $\chi^2/2$ distribution rather than χ^2 . As such, the 95% C.L. upper limits on the cross section $\langle \sigma v \rangle_{\text{UL}}$ are given when the $\Delta \log \mathcal{L}_{\text{st}}(\alpha_{i,j} | \langle \sigma v \rangle, J) \sim -3.8/2$.

C. dN/dz measurement

In this Subsection, according to the method described in Subsection II B, we measure the dN/dz distribution of the HSC-LSBG sample. We divide the reference redshift sample into five equally separated bins from $z = 0$ to 0.15. Then we take the cross correlation between the sample in each bin and the entire LSBG sample. The angular cross correlation is computed by the estimator [52] in angular bins of $0.1^\circ < \theta < 1.0^\circ$, logarithmically uniformly sampled,

$$w(z_i, \theta_j) = \frac{D_p D_{s,i} - D_p R_{s,i} - R_p D_{s,i} + R_p R_{s,i}}{R_p R_{s,i}}, \quad (11)$$

where DD or DR represent the normalized number of pairs separated within the j -th angular bin between data and data or data and random, respectively. Subscripts p, s and i represent the photometric sample and reference sample in the i -th redshift bin, respectively. We omit the argument of θ_j on the right hand side where no confusion arises. For the spec- z samples, we apply the weight developed by [53] for a rigorous optimal variance with the galaxy power spectrum,

$$w_{\text{FKP}}(\mathbf{r}) = \frac{1}{1 + n(\mathbf{r})P_0} \quad (12)$$

where $P_0 = 1000h^{-3}\text{Mpc}^3$ is the amplitude of the power spectrum at the scale where the variance is optimal and

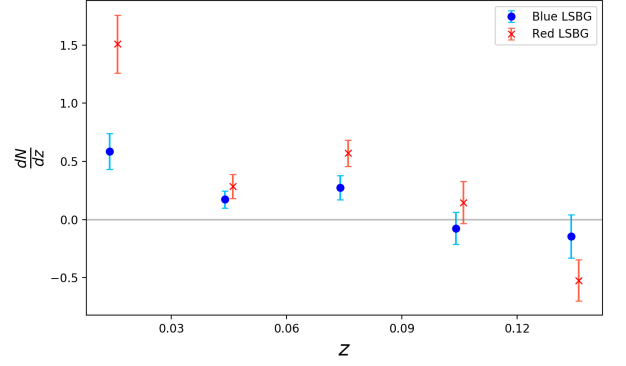


FIG. 1. The dN/dz of blue (blue colored) and red (red colored) HSC-LSBGs. Note that error bars present 2- σ level of an uncertainty by considering error estimation of the Jackknife subsampling for the angular cross-correlation of HSC-LSBGs with NSA samples.

$n(\mathbf{r})$ is the comoving number density of samples at the position.

To estimate the covariance of w , we use the Jackknife subsampling method [54]. We divide the HSC-LSBG and NSA samples into 100 subregions where individual regions have independent $\sim 2 \text{ deg}^2$ sky coverage. The covariance matrix C_{ij}^z is defined by

$$C_{ij}^z = \frac{M-1}{M} \sum_{k=1}^M [w_k(z, \theta_i) - \hat{w}(z, \theta_i)] [w_k(z, \theta_j) - \hat{w}(z, \theta_j)], \quad (13)$$

where $w_k(z, \theta_i)$ is the angular correlation measurement for the k -th Jackknife sub-sample and M is the number of the Jackknife sub-samples, $M = 100$. \hat{w} is the averaged correlation function over all jackknife sub-samples,

$$\hat{w}(z, \theta_i) = \frac{1}{M} \sum_{k=1}^M w_k(z, \theta_i). \quad (14)$$

When converting $\bar{w}(z_i)$ to dN_p/dz in Equation 6, we assume that the linear bias of the spec- z samples is unity. Figure 1 represents the dN/dz distribution measurement. The errors are measured using the Jackknife resampling implemented in the `treecorr` [55].

D. Evaluation of statistical uncertainty

To evaluate statistical uncertainties for $\langle \sigma v \rangle_{\text{UL}}$ in the composite analysis, we consider uncertainties of halo mass and concentration parameter as well as the dN/dz measurement error on 500 Monte Carlo simulations. First, for the halo mass, we evaluate its uncertainty as $\Delta \log M_{\text{halo}} = 0.8$ at 1- σ Gaussian error by computing the scatter of stellar-to-halo-mass conversion. In addition, we adopt a concentration parameter error of $\Delta \log c$

of 0.1 at $1\text{-}\sigma$ Gaussian error [56]. Accordingly, the total uncertainty for halo properties results in J -factor uncertainties of ~ 0.9 dex at $1\text{-}\sigma$ error. Moreover, we randomly assign the distance to galaxies according to this distribution; therefore, the negative values of the probability are strictly prohibited. Thus, in our analysis, the amplitude in each redshift bin is considered a free parameter, and we provide the confidence intervals based on the posterior distribution. Given that the measurement gives the likelihood of the form of the Gaussian, $P(\alpha_i|D) \propto \exp[-(\alpha_i - \hat{\alpha}_i)^2 / 2\hat{\sigma}_i^2]$, where $\hat{\cdot}$ variables are measurement. Then the stepwise prior, $P(\alpha_i) = 0$ for $\alpha_i < 0$ and 1 otherwise is applied. Further, we compute the maximum α_i and 95 percentiles from the posterior distribution $P(\alpha_i|D)P(\alpha_i)$. We finally apply linear interpolation between each center of redshift bin to the posterior distribution. We take a conservative limit of the minimum redshift of the sample corresponding to 25 Mpc, which is the minimum distance among the HSC-LSBG samples with precisely measured distance.

In Figure 2, we show the total J -factor values as a function of the number of stacked objects, N_{st} . In the order of square, cross and circle symbols, the error-bars plot the total values including dN/dz measurement uncertainty, halo property and both, respectively. For comparison with relevant works for probing constraint on the DM annihilation cross-section, we display $\langle\sigma v\rangle_{\text{UL}}$ with 95% C.L. for DM mass of 1 TeV in the right axis, which corresponds to the J -factor value on the left axis. Note that when converting J -factor to $\langle\sigma v\rangle_{\text{UL}}$, we apply a mean flux of our UGRB sky. The upper limit is affected by both the fluctuation and target's J -factor value, however we find that, even in the lower energy regime, the scatter by the fluctuation is smaller (~ 0.4 dex at $2\text{-}\sigma$ level) than the total halo property and dN/dz measurement uncertainty.

IV. DISCUSSION

A. Correlation between neighbors

We performed the composite analysis in Subsection IIIB assuming that the likelihood functions of individual objects are independent of each other. Such correlations are expected when the number density of the sample is high because the PSF of *Fermi*-LAT is $\sim 1^\circ$. In this Subsection, we demonstrate that the correlation between data at different points can be negligible.

In the HSC-*Fermi* sky coverage, we select 10 independent patches with the size of $10 \times 10 \text{ deg}^2$. From each patch, we randomly select 60 pairs of points with separations of 0.5° to 3° . To evaluate the correlation between the putative flux amplitudes of the paired objects, we perform the joint likelihood analysis for the pairs, which simultaneously optimizes the fluxes of the paired objects.

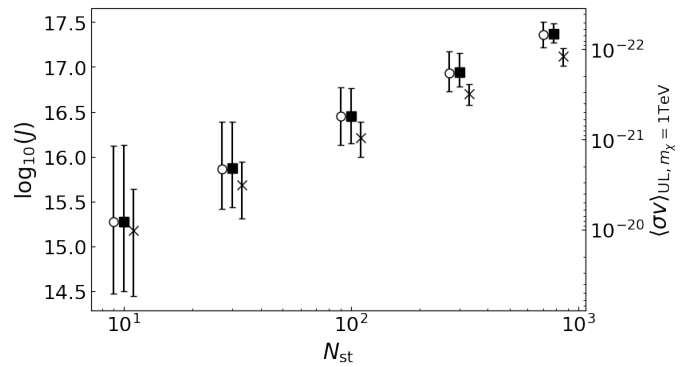


FIG. 2. Total J -factor values of HSC-LSBG summed over N_{st} samples taken randomly from 781 samples. The error bar with filled square includes dN/dz measurement uncertainty, cross symbol includes halo property uncertainty and circle symbol includes both. Each error bar shows 95% confidence region based on 500 Monte Carlo simulations. The right axis shows $\langle\sigma v\rangle_{\text{UL}}$ for DM mass of 1 TeV with 95% C.L. corresponding to J -factor value in the left axis.

The putative flux of an object is parameterized as

$$\frac{d\Phi}{dE} = \alpha \left(\frac{E}{1000[\text{MeV}]} \right)^{-2}. \quad (15)$$

Figure 3 shows the absolute value of the correlation between two amplitude parameters as the function of the separation. The error-bars are computed from the 60 independent pairs that reflects the fluctuations of the residual gamma-ray flux. The cross-covariance is normalized by the diagonal terms, i.e., $\rho_{i,j} \equiv \text{cov}(\alpha_i, \alpha_j) / \sigma_i \sigma_j$. Although we expect strong correlation on scales smaller than 1 deg. because of the PSF size of *Fermi*-LAT, the correlation at the smallest separation, which corresponds to the HSC-LSBG mean separation, the correlation is less than 0.1 at $1\text{-}\sigma$ level. We note that all the cross correlation is negative at all scales, which is the consequence of the conservation of the total flux. For further validation, we perform a composite likelihood analysis in which we obtain the likelihood profiles for putative fluxes of all samples within a single LAT data patch simultaneously. Figure 4 compares the $\langle\sigma v\rangle_{\text{UL}}$ constraints with this simultaneous approach ('simultaneous' case) with the one obtained based on the assumption that all objects are independent of each other ('independent' case). We emphasize that the 'independent' case provides a weaker constraint on $\langle\sigma v\rangle_{\text{UL}}$ than the 'simultaneous' case. This is because the total flux conservation is imposed, which results in the larger putative flux amplitude in the 'independent' case than 'simultaneous' case. Note that in this calculation, we set all objects' J -factor to $10^{14.5} \text{ GeV}^2/\text{cm}^5$ and choose a specific dN/dz , therefore, the amplitudes of $\langle\sigma v\rangle_{\text{UL}}$ in Figure 4 do not correspond to the ones in Figure 2.

We conclude that the correlation between neighboring points is less than 10%, on scales 0.5 deg. and even if

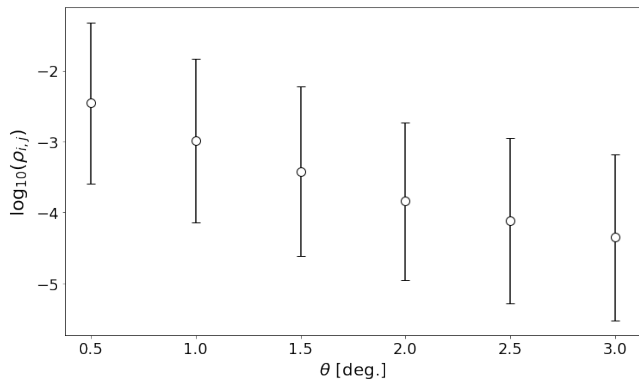


FIG. 3. The off-diagonal value of covariance matrix between two amplitude parameters for each paired objects as a function of separation angles. The error bars represent $1\text{-}\sigma$ errors of the off-diagonals with 60 pairs in each angular bin.

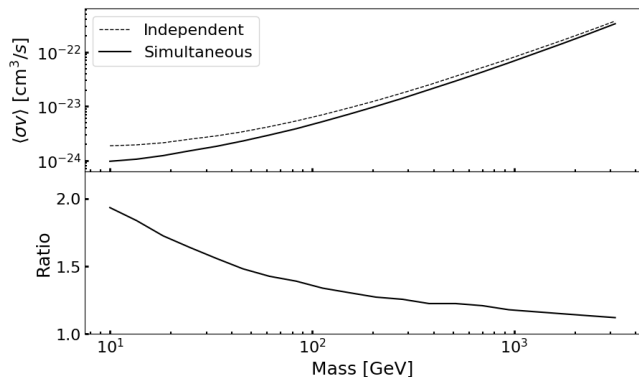


FIG. 4. (Top) The difference between $\langle\sigma v\rangle_{\text{UL}}$ in the composite analysis with all LSBGs in the simultaneous approach (solid line) and the one with assumption of flux likelihood profiles of all LSBGs being independent of each other (dotted line) as a function of DM mass. (Bottom) The ratio of the upper limits in the two cases.

we ignore the correlation, which is computationally much less expensive, we will obtain the conservative constraints on the $\langle\sigma v\rangle_{\text{UL}}$.

B. The power of stacking

In this Subsection, we discuss a scaling relation of the statistical power on $\langle\sigma v\rangle_{\text{UL}}$ as a function of the number of stacking, under the low background photon limit. We will show that $\langle\sigma v\rangle_{\text{UL}}$ becomes more stringent proportional to the N_{st} at high mass limit but scales as $\sqrt{N_{\text{st}}}$ at low mass ranges. We will also show that this scaling relation converges to N_{st} whatever the DM mass if the N_{st} is sufficiently large.

First, we revisit a Poisson likelihood for a single LSBG in the UGRB. The likelihood function for model param-

eters is given by the Poisson distribution,

$$\mathcal{L} = \prod_i \frac{\lambda_i^{n_i} e^{-\lambda_i}}{n_i!}, \quad (16)$$

where the index i runs over all energy bins and pixels and n_i is the observed photon counts; λ_i is expected photon counts for model fluxes, which is decomposed into the Galactic foreground, isotropic background and resolved point-source model fluxes as well as the flux by the DM annihilation for the single LSBG. A UGRB sky is derived from the modeling of all the γ -ray sources except for the LSBG flux as described in Section III A 4. Therefore, fixing the model parameters Θ of the background sky, λ_i depends only on the single parameter, $\langle\sigma v\rangle$. We denote $\lambda_i = \lambda_i^{\text{others}}(\Theta) + \lambda_i^T(\langle\sigma v\rangle)$, where $\lambda_i^{\text{others}}$ is the total model flux of all sources without LSBG and λ_i^T is the model flux of LSBG. For simplicity, we consider that all LSBGs have the same J-factor, which means that their model fluxes are equal. In addition, we consider the fact that, in energy regimes higher than ~ 30 GeV, the LAT hardly detects photons. Given that there is no photon count ($n_i = 0$) in such energy regimes and in all pixels, we expect $\lambda_i^{\text{others}}(\mu) = 0$ and then $\log \mathcal{L} = -\sum_i \lambda_i^T(\langle\sigma v\rangle)$.

Consequently, we obtain the composite likelihood with N_{st} objects using Equation 8,

$$\Delta \log \mathcal{L}_{\text{st}} = -N_{\text{st}} \sum_i \lambda_i^T(\langle\sigma v\rangle), \quad (17)$$

where N_{st} is the number of objects in the composite analysis. Therefore, in our criteria the upper limit is proportional to $1/N_{\text{st}}$ because of $\lambda_i^T(\langle\sigma v\rangle) \propto \langle\sigma v\rangle$.

In Figure 5, we show the ratio of $\langle\sigma v\rangle_{\text{UL}}$ with N_{st} objects to the one with a single object for DM mass of 10 GeV, 100 GeV and 1 TeV. With N_{st} larger than ~ 30 , the upper limits scale with the inverse of N_{st} for all mass ranges. For DM mass of 100 GeV and 1 TeV, this scaling relation is seen, even in smaller N_{st} . This behavior is reasonable, considering the photon-count statistics in a high energy regime. The annihilation process with more massive DM particles can produce higher energy photons, thus probing the DM annihilation for more massive DM is affected by photon-count statistics in high energy regimes.

V. SUMMARY

In this study, we proposed to take a cross correlation between γ -ray sky and potential γ -ray sources with unknown redshifts for probing the DM annihilation signal. The most important point is that we do not need to measure the individual distance to the γ -ray sources but the overall redshift distribution is sufficient to constrain the DM annihilation cross section. By applying the redshift clustering method, we obtained a redshift distribution of total samples instead of redshifts of individual objects and then we randomly assigned the distance to

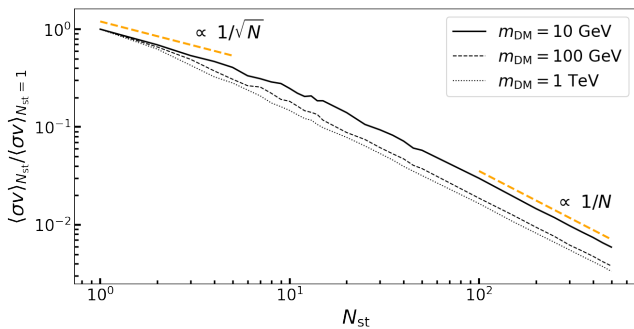


FIG. 5. Scaling relation of $\langle\sigma v\rangle_{\text{UL}}$ with a number of objects N_{st} in the composite analysis. The vertical axis is the ratio of the upper limit with N_{st} objects to the one with a single object. The black solid, dashed and dotted lines correspond to the ratio for DM mass of 10 GeV, 100 GeV and 1 TeV, respectively. Scaling with $1/N_{\text{st}}$ and $1/\sqrt{N_{\text{st}}}$ are shown in orange dashed lines.

each LSBG according to this distribution. To validate the proposed method, we measured dN/dz of full samples of the HSC-LSBG catalog including ~ 800 objects and constrained the DM annihilation cross-section via a composite likelihood analysis with all LSBGs given distances by the procedure and UGRB constructed from eight-year *Fermi*-LAT observation data.

In the dN/dz measurement for LSBG samples, we employed the NSA catalog as spec- z samples in overlapped regions with the HSC region. The uncertainty in the dN/dz is evaluated by the Monte Carlo simulation and we found that the uncertainty on the upper limit is quite small in the composite analysis with ~ 1000 objects. Therefore, using dN/dz distribution of overall target samples instead of the individual sample's redshifts is a valid and robust approach for the DM signal search.

To reduce the computational cost, we applied an assumption that all flux model parameters for different LSBGs are independent of each other. The number density of the LSBGs ($\sim 0.5^\circ$) was comparable to the LAT PSF scale, which may lead to a correlation between flux model parameters for neighboring LSBGs, and thus may break the assumption. We validated the assumption in two ways. First, we computed covariance matrix between two flux amplitude parameters for each paired neighbor and confirmed that off-diagonals of the correlation matrix was smaller than 0.1 at the separation angle 0.5° . Second, fixing the J-factor and distance to each object ,

we performed a composite likelihood analysis in which we obtained the likelihood profiles for putative fluxes of all samples in each LAT patch simultaneously. By comparing $\langle\sigma v\rangle_{\text{UL}}$, we found that the constraints differs at most factor of 2. Moreover, if we take the data independently, the constraints become more conservative due to the relaxation of the total flux conservation condition. This means that even if we ignore the correlation among the data, particularly due to the reduction of the computational cost, we do not need to worry about the artificial constraint.

Finally, we found the scaling relation of $\langle\sigma v\rangle_{\text{UL}}$ with the number of objects N_{st} in the composite likelihood analysis. Under an assumption of no observed photon, we found that $\langle\sigma v\rangle_{\text{UL}}$ is proportional to $1/N_{\text{st}}$ analytically. In addition, using the HSC-LSBGs, we computed the scaling for DM mass of 10 GeV, 100 GeV and 1 TeV and showed that for all DM masses the upper limit scales with $1/N_{\text{st}}$ using $N_{\text{st}} \gtrsim 30$. This is the significant effect which is the consequence of the Poisson statistics and is different from the Gaussian statistics in which the scaling obeys $1/\sqrt{N_{\text{st}}}$.

In future imaging surveys with next-generation telescopes such as the LSST, a huge amount of LSBGs will be detected because of wider sky coverage and better sensitivity. For example, LSST has a sky coverage of $\sim 20,000 \text{ deg}^2$ and reaches the depth of $\sim 27.5 \text{ mag/arcsec}^2$ in i band and consequently has the potential to discover $\mathcal{O}(10^5)$ objects. Although, as the reference samples, we need spec- z or high-precision photo- z samples located in the local universe covering such a wide sky, it is expected to decrease uncertainties for estimate of $\langle\sigma v\rangle_{\text{UL}}$ due to dN/dz measurement and halo properties. Moreover, by increasing statistics, we can realize a more detailed dN/dz measurement, particularly a redshift range corresponding to distance of less than 25 Mpc which is the minimum distance adopted for conservative J-factor estimate in our likelihood procedure. This will give a more stringent constraint on the cross-section beyond simple scaling with $1/N_{\text{st}}$.

ACKNOWLEDGMENTS

This work was supported in part by World Premier International Research Center Initiative, MEXT, Japan, and JSPS KAKENHI Grant No. 19H00677, 20H05850, 20H05855 and 20J11682.

-
- [1] G. Jungman, M. Kamionkowski, and K. Griest. Supersymmetric dark matter. *Physics Report*, 267:195–373, Mar 1996.
 - [2] Gianfranco Bertone, Dan Hooper, and Joseph Silk. Particle dark matter: evidence, candidates and constraints. *Physics Report*, 405(5-6):279–390, Jan 2005.

- [3] Giorgio Arcadi, Maíra Dutra, Pradipta Ghosh, Manfred Lindner, Yann Mambrini, Mathias Pierre, Stefano Profumo, and Farinaldo S. Queiroz. The waning of the WIMP? A review of models, searches, and constraints. *European Physical Journal C*, 78(3):203, March 2018.
- [4] Leszek Roszkowski, Enrico Maria Sessolo, and Sebas-

- tian Trojanowski. WIMP dark matter candidates and searches—current status and future prospects. *Reports on Progress in Physics*, 81(6):066201, Jun 2018.
- [5] Tongyan Lin. TASI lectures on dark matter models and direct detection. *arXiv e-prints*, page arXiv:1904.07915, Apr 2019.
- [6] Gary Steigman, Basudeb Dasgupta, and John F. Beacom. Precise relic wimp abundance and its impact on searches for dark matter annihilation. *Phys. Rev. D*, 86:023506, Jul 2012.
- [7] The Fermi-LAT collaboration. Fermi Large Area Telescope Fourth Source Catalog. *arXiv e-prints*, page arXiv:1902.10045, Feb 2019.
- [8] K. Belotsky, A. Kirillov, and M. Khlopov. Gamma-ray evidence for dark matter clumps. *Gravitation and Cosmology*, 20(1):47–54, Jan 2014.
- [9] C. Gordon and O. Macías. Dark matter and pulsar model constraints from Galactic Center Fermi-LAT gamma-ray observations. *Phys. Rev. D*, 88(8):083521, October 2013.
- [10] K. N. Abazajian, N. Canac, S. Horiuchi, and M. Kaplinghat. Astrophysical and dark matter interpretations of extended gamma-ray emission from the Galactic Center. *Phys. Rev. D*, 90(2):023526, July 2014.
- [11] F. Calore, I. Cholis, and C. Weniger. Background model systematics for the Fermi GeV excess. *JCAP*, 3:038, March 2015.
- [12] T. Daylan, D. P. Finkbeiner, D. Hooper, T. Linden, S. K. N. Portillo, N. L. Rodd, and T. R. Slatyer. The characterization of the gamma-ray signal from the central Milky Way: A case for annihilating dark matter. *Physics of the Dark Universe*, 12:1–23, June 2016.
- [13] Ackermann, M. *et al.* The Fermi Galactic Center GeV Excess and Implications for Dark Matter. *Astrophys. J.*, 840(1):43, May 2017.
- [14] Shin’ichiro Ando, Aurélien Benoit-Lévy, and Eiichiro Komatsu. Mapping dark matter in the gamma-ray sky with galaxy catalogs. *Phys. Rev. D*, 90(2):023514, Jul 2014.
- [15] Ackermann, M. *et al.* The Spectrum of Isotropic Diffuse Gamma-Ray Emission between 100 MeV and 820 GeV. *Astrophys. J.*, 799:86, January 2015.
- [16] Ajello, M. *et al.* The Origin of the Extragalactic Gamma-Ray Background and Implications for Dark Matter Annihilation. *Astrophys. J.*, 800(2):L27, Feb 2015.
- [17] J. Kataoka, M. Tahara, T. Totani, Y. Sofue, Y. Inoue, S. Nakashima, and C. C. Cheung. Global Structure of Isothermal Diffuse X-Ray Emission along the Fermi Bubbles. *Astrophys. J.*, 807(1):77, Jul 2015.
- [18] Ackermann, M. *et al.* Unresolved Gamma-Ray Sky through its Angular Power Spectrum. *Phys. Rev. Lett.*, 121(24):241101, Dec 2018.
- [19] Daiki Hashimoto, Atsushi J. Nishizawa, Masato Shirasaki, Oscar Macias, Shunsaku Horiuchi, Hiroyuki Tashiro, and Masamune Oguri. Measurement of redshift-dependent cross-correlation of HSC clusters and Fermi γ -rays. *MNRAS*, 484(4):5256–5266, Apr 2019.
- [20] Charles Thorpe-Morgan, Denys Malyshev, Christoph-Alexander Stegen, Andrea Santangelo, and Josef Jochum. Annihilating dark matter search with 12 yr of Fermi LAT data in nearby galaxy clusters. *MNRAS*, 502(3):4039–4047, April 2021.
- [21] Ackermann, M. *et al.* Searching for Dark Matter Annihilation from Milky Way Dwarf Spheroidal Galaxies with Six Years of Fermi Large Area Telescope Data. *Phys. Rev. Lett.*, 115(23):231301, Dec 2015.
- [22] Albert, A. *et al.* Searching for Dark Matter Annihilation in Recently Discovered Milky Way Satellites with Fermi-Lat. *Astrophys. J.*, 834(2):110, Jan 2017.
- [23] V. Gammaldi, E. Karukes, and P. Salucci. Theoretical predictions for dark matter detection in dwarf irregular galaxies with gamma rays. *Phys. Rev. D*, 98(8):083008, Oct 2018.
- [24] S. Hoof, A. Geringer-Sameth, and R. Trotta. A Global Analysis of Dark Matter Signals from 27 Dwarf Spheroidal Galaxies using Ten Years of Fermi-LAT Observations. *arXiv e-prints*, December 2018.
- [25] Kimberly K. Boddy, Jason Kumar, Danny Marfatia, and Pearl Sandick. Model-independent constraints on dark matter annihilation in dwarf spheroidal galaxies. *Phys. Rev. D*, 97(9):095031, May 2018.
- [26] Sebastian Hoof, Alex Geringer-Sameth, and Roberto Trotta. A global analysis of dark matter signals from 27 dwarf spheroidal galaxies using 11 years of Fermi-LAT observations. *JCAP*, 2020(2):012, February 2020.
- [27] Daiki Hashimoto, Oscar Macias, Atsushi J. Nishizawa, Kohei Hayashi, Masahiro Takada, Masato Shirasaki, and Shin’ichiro Ando. Constraining dark matter annihilation with HSC low surface brightness galaxies. *JCAP*, 2020(1):059, January 2020.
- [28] Carolin Wittmann, Thorsten Lisker, Liyuaalem Ambachew Tilahun, Eva K. Grebel, Christopher J. Conselice, Samantha Penny, Joachim Janz, John S. Gallagher, Ralf Kotulla, and James McCormac. A population of faint low surface brightness galaxies in the Perseus cluster core. *MNRAS*, 470(2):1512–1525, Sep 2017.
- [29] Wei Du, Cheng Cheng, Hong Wu, Ming Zhu, and Yougang Wang. Low Surface Brightness Galaxy catalogue selected from the α 40-SDSS DR7 Survey and Tully-Fisher relation. *MNRAS*, 483(2):1754–1795, Feb 2019.
- [30] D. J. Prole, M. Hilker, R. F. J. van der Burg, M. Cantiello, A. Venhola, E. Iodice, G. van de Ven, C. Wittmann, R. F. Peletier, S. Mieske, M. Capaccioli, N. R. Napolitano, M. Paolillo, M. Spavone, and E. Valentijn. Halo mass estimates from the globular cluster populations of 175 low surface brightness galaxies in the Fornax cluster. *MNRAS*, 484(4):4865–4880, Apr 2019.
- [31] J. P. Greco, J. E. Greene, M. A. Strauss, L. A. Macarthur, X. Flowers, A. D. Goulding, S. Huang, J. H. Kim, Y. Komiyama, A. Leauthaud, L. Leisman, R. H. Lupton, C. Sifón, and S.-Y. Wang. Illuminating Low Surface Brightness Galaxies with the Hyper Suprime-Cam Survey. *Astrophys. J.*, 857:104, April 2018.
- [32] Jeffrey A. Newman. Calibrating Redshift Distributions beyond Spectroscopic Limits with Cross-Correlations. *Astrophys. J.*, 684(1):88–101, September 2008.
- [33] Brice Ménard, Ryan Scranton, Samuel Schmidt, Chris Morrison, Donghui Jeong, Tamas Budavari, and Mubdi Rahman. Clustering-based redshift estimation: method and application to data. *arXiv e-prints*, page arXiv:1303.4722, March 2013.
- [34] Gatti, M. *et al.* Dark Energy Survey Year 3 Results: Clustering Redshifts – Calibration of the Weak Lensing Source Redshift Distributions with redMaGiC and BOSS/eBOSS. *arXiv e-prints*, page arXiv:2012.08569, December 2020.
- [35] Tesla E. Jeltema and Stefano Profumo. Fitting the Gamma-Ray Spectrum from Dark Matter with DM-FIT: GLAST and the Galactic Center Region. *JCAP*,

- 0811:003, 2008.
- [36] N. Hiroshima, S. Ando, and T. Ishiyama. Modeling evolution of dark matter substructure and annihilation boost. *Phys. Rev. D*, 97(12):123002, June 2018.
 - [37] J. F. Navarro, C. S. Frenk, and S. D. M. White. The Structure of Cold Dark Matter Halos. *Astrophys. J.*, 462:563, May 1996.
 - [38] Benedikt Diemer and Michael Joyce. An Accurate Physical Model for Halo Concentrations. *Astrophys. J.*, 871(2):168, February 2019.
 - [39] Benedikt Diemer. COLOSSUS: A Python Toolkit for Cosmology, Large-scale Structure, and Dark Matter Halos. *ApJS*, 239(2):35, December 2018.
 - [40] Jester, S. *et al.* The Sloan Digital Sky Survey View of the Palomar-Green Bright Quasar Survey. *AJ*, 130:873–895, September 2005.
 - [41] J. Woo, S. Courteau, and A. Dekel. Scaling relations and the fundamental line of the local group dwarf galaxies. *MNRAS*, 390:1453–1469, November 2008.
 - [42] B. P. Moster, T. Naab, and S. D. M. White. Galactic star formation and accretion histories from matching galaxies to dark matter haloes. *MNRAS*, 428:3121–3138, February 2013.
 - [43] Michael R. Blanton, Eyal Kazin, Demitri Muna, Benjamin A. Weaver, and Adrian Price-Whelan. Improved Background Subtraction for the Sloan Digital Sky Survey Images. *AJ*, 142(1):31, July 2011.
 - [44] Miyazaki, S. *et al.* Hyper Suprime-Cam: System design and verification of image quality. *PASJ*, 70:S1, January 2018.
 - [45] Komiyama, Y. *et al.* Hyper Suprime-Cam: Camera dewar design. *PASJ*, 70:S2, January 2018.
 - [46] Aihara, Hiroaki *et al.* Second data release of the Hyper Suprime-Cam Subaru Strategic Program. *PASJ*, 71(6):114, December 2019.
 - [47] Atwood, W. *et al.* Pass 8: Toward the Full Realization of the Fermi-LAT Scientific Potential. *arXiv e-prints*, page arXiv:1303.3514, March 2013.
 - [48] Ackermann, M. *et al.* The Fermi Large Area Telescope on Orbit: Event Classification, Instrument Response Functions, and Calibration. *ApJS*, 203:4, November 2012.
 - [49] M. Wood, R. Caputo, E. Charles, M. Di Mauro, J. Magill, J. S. Perkins, and Fermi-LAT Collaboration. Fermipy: An open-source Python package for analysis of Fermi-LAT Data. *International Cosmic Ray Conference*, 301:824, Jan 2017.
 - [50] O. Helene. Upper limit of peak area. *Nuclear Instruments and Methods in Physics Research*, 212(1-3):319–322, Jul 1983.
 - [51] Nolan, P. L. *et al.* Fermi Large Area Telescope Second Source Catalog. *ApJS*, 199(2):31, Apr 2012.
 - [52] S. D. Landy and A. S. Szalay. Bias and variance of angular correlation functions. *Astrophys. J.*, 412:64–71, July 1993.
 - [53] Hume A. Feldman, Nick Kaiser, and John A. Peacock. Power-Spectrum Analysis of Three-dimensional Redshift Surveys. *Astrophys. J.*, 426:23, May 1994.
 - [54] Scranton, R. *et al.* Analysis of Systematic Effects and Statistical Uncertainties in Angular Clustering of Galaxies from Early Sloan Digital Sky Survey Data. *Astrophys. J.*, 579:48–75, November 2002.
 - [55] Mike Jarvis. TreeCorr: Two-point correlation functions, August 2015.
 - [56] A. A. Dutton and A. V. Macciò. Cold dark matter haloes in the Planck era: evolution of structural parameters for Einasto and NFW profiles. *MNRAS*, 441:3359–3374, July 2014.